Local electronic structure and nanolevel hierarchical organization of bone tissue: theory and NEXAFS study

2016 Nanotechnology 27 504002

(http://iopscience.iop.org/0957-4484/27/50/504002)

IOP Publishing Nanotechnology
Nanotechnology 27 (2016) 504002 (8pp) doi:10.1088/0957-4484/27/50/504002

Local electronic structure and nanolevel hierarchical organization of bone tissue: theory and NEXAFS study

A A Pavlychev[1], A S Avrunin[2], A S Vinogradov[1], E O Filatova[1], A A Doctorov[3], Yu S Krivosenko[1], D O Samoilenko[1], G I Svirskiy[1], A S Konashuk[1] and D A Rostov[1]

[1] Solid State Electronics Department, St. Petersburg State University, St. Petersburg, 198504, Russian Federation
[2] Vreden Russian Research Institute of Traumatology and Orthopedics, St. Petersburg, 195427, Russian Federation
[3] All-Russian Research Institute of Medicinal and Aromatic Plants, Moscow, 117216, Russian Federation

E-mail: andrey.pavlychev@gmail.com

Received 15 June 2016
Accepted for publication 28 October 2016
Published 22 November 2016

Abstract

Theoretical and experimental investigations of native bone are carried out to understand relationships between its hierarchical organization and local electronic and atomic structure of the mineralized phase. The 3D superlattice model of a coplanar assembly of the hydroxyapatite (HAP) nanocrystallites separated by the hydrated nanolayers is introduced to account the interplay of short-, long- and super-range order parameters in bone tissue. The model is applied to (i) predict and rationalize the HAP-to-bone spectral changes in the electronic structure and (ii) describe the mechanisms ensuring the link of the hierarchical organization with the electronic structure of the mineralized phase in bone. To check the predictions the near-edge x-ray absorption fine structure (NEXAFS) at the Ca 2p, P 2p and O 1s thresholds is measured for native bone and compared with NEXAFS for reference compounds. The NEXAFS analysis has demonstrated the essential hierarchy induced HAP-to-bone red shifts of the Ca and P 2p-to-valence transitions. The lowest O 1s excitation line at 532.2 eV in bone is assigned with superposition of core transitions in the hydroxide $OH^{-}(H_2O)_m$ anions, $Ca^{2+}(H_2O)_n$ cations, the carboxyl groups inside the collagen and $[PO_4]^{2-}$ and $[PO_4]^{-}$ anions with unsaturated P–O bonds.

Keywords: bone, mineral matrix, hydroxyapatite, superlattice, NEXAFS, hierarchical matter

(Some figures may appear in colour only in the online journal)

1. Introduction

Bone is one of the most intriguing hierarchical materials in nature. Having relatively simple building blocks its hierarchical structuring provides fascinating mechanical and biological properties as well as high material functionality [1–9]. Studying how bone is built up and applying the knowledge to develop cutting-edge technologies one can realize the advanced materials [3].

Material science, biological and medical investigations trace the complicated hierarchy of the skeleton designs from macro- to nano-level and disclose up to seven hierarchical levels of bone organization [1–10]. Nanolevel research of bones encounters great difficulty because electronic and atomic structure of their nanoblocks is not sufficiently studied. This gap prevents solutions of many fundamental and applied problems such as bio-design of advanced materials [3–12], control and fine-tuning of ion exchange and age-related processes in bones [10], paleontological research [13, 14] as well as development of *in vivo* models [15].

Being a composition of hard hydroxyapatite (HAP, $Ca_{10}(PO_4)_6(OH)_2$) plates with flexible collagen molecules,

bone tissue becomes respectively more elastic and firm [3–6] in comparison with the parent mineral and the collagen. The mineralized plates are distributed among the collagen fibrils and reproduce their spiral shape [3–6, 9]. The third basic component is water throughout the bone tissue [1, 4, 6]. Its role in the nanodynamics and nanoelectronics of bone is not completely understood [1, 5, 16–18]. It is known that the stretching differs in hydrated and dehydrated fibrils [11]; the water largely determines thermal and mechanical properties of bone [18–20] and provides its high ionic mobility [7].

The electronic and atomic structure of the perfect-crystal HAP is well studied. The band theory describes HAP as the wide-band-gap insulator in the range of ~5 eV [21, 22]. The bonding studies indicate that the crystal is determined by the sets of $[PO_4]^{3-}$ and Ca^{2+} channels populated by columns of OH^- anions [21]. The crystallographic cell of HAP in the form of rectangular parallelepiped is shown in the lower panel of figure 1. Strong ionic conductivity of HAP is assigned to high mobility of hydroxyl ions in the crystal lattice. Considering the electronic and atomic structure of the perfect-crystal HAP as a ground level we bring out the main structural peculiarities inherent to native bones and investigate the interplay of the ground level with the upper hierarchical ones. Our particular interest is to reveal the mechanisms linking the hierarchical levels and to describe them.

Both transmission electron microscopic and small angle x-ray scattering methods extensively applied to bones make evident that intra- and inter-fibrilar associations of the crystallites form a series of parallel and spiral wound mineralized plates [5, 23, 24] as exhibited in figure 1 (upper panel). These plates are usually approximated as coplanar assemblies of the nanocrystallites of HAP [3, 23, 24]. This assembly is shown in the middle panel of figure 1. It is seen that the nanocrystallites are separated one from the other by nanolayers of saturated aqueous solution containing mainly the anions OH^-, $[PO_4]^{3-}$ and $[CO_3]^{2-}$ and dications Ca^{2+} [7]. The morphological picture in figure 1 is a result of the structural and functional relationship between adjacent levels of the hierarchical organization of bone. Size distribution of the crystallites in the mineralized phase is age-related [17, 25, 26] and depends on atomic incorporations and substitutions [19, 24, 27, 28].

To date, many efforts have been invested to investigate the effect of chemical composition on electronic properties of bone tissue both theoretically and experimentally. In particular, the near edge x-ray absorption fine structure (NEXAFS) spectroscopy providing a sensitive probing of local electron structure in matter [29, 30] is also applied to bones [31–36]. However the influence of the hierarchical organization on the properties is practically left unattended.

Our attention is put on core-to-valence transitions near the Ca 2p, P 2p and O 1s edges in native bone to visualize the effect of its hierarchical organization on its local electronic states. In the work we present our theoretical and experimental investigations of native bone aimed to understand the interplay of the lowest hierarchical levels plotted in figure 1. We focus on electronic and atomic structure of the mineralized phase, as collagen constituting 95% of all organic

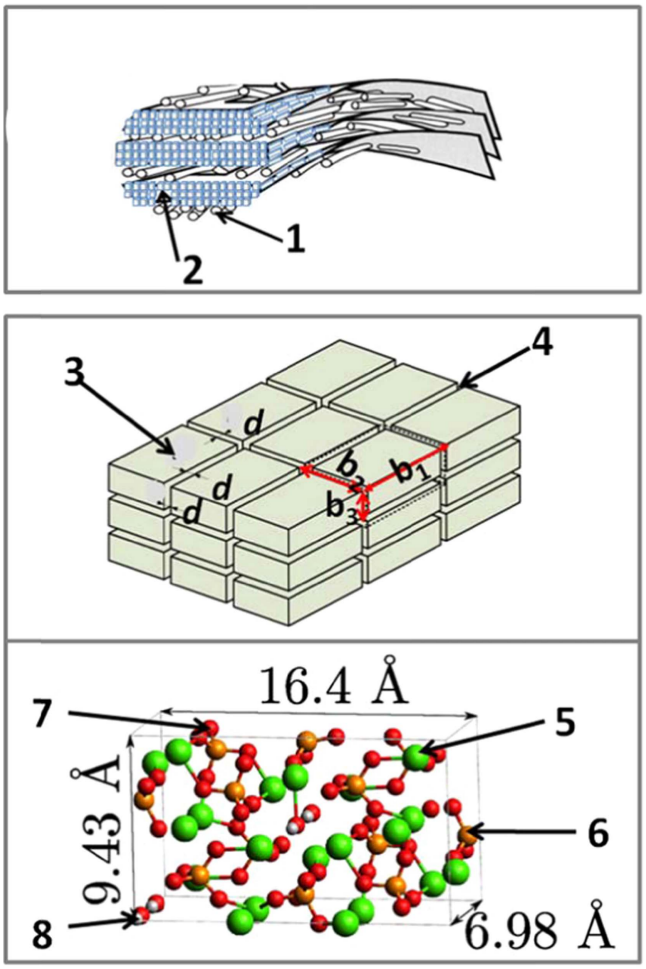

Figure 1. The three lowest hierarchical levels in the mineralized phase of bone tissue are shown schematically. Upper panel: the mineralized plates (2) distributed among the collagen molecules (1) are swirling around a fibril (not shown here) [23, 24]. Middle panel: the coplanar assembly of the nanocrystallite (3) separated by the hydrated layers (4). The basic vectors of superlattice translation $\boldsymbol{b_j}$ are shown. Low panel: the crystallographic rectangular cell of HAP with the parameters $a = 9.43$ Å, $b = 16.33$ Å, $c = 6.98$ Å. Arrows 5–8 point at Ca, P, O and H atoms shown with green, orange, red and gray, respectively.

phase in bone and being the main structural protein is studied in more detail (see, e.g. [3, 11]).

The mineralized phase is conventionally regarded as a nanostructured HAP (or carbonized apatite or bioapatite) with low crystallinity [1, 14]. In section 2, the novel 3D-superlattice (3DSL) of 'black-boxes-in-muddy-waters' model is introduced to describe the electronic structure of the mineralized phase and to understand how its hierarchical organization disturbs the structure. The model shows that the hierarchy induced changes in electronics of native bone are closely related with the size of the nanocrystallites. To visualize the hierarchy effects on electronic structure, the high resolution x-ray absorption measurements near the Ca and P 2p and O 1s edges in native bone are performed and described in section 3. In section 4, the NEXAFS spectra of native bone are examined and compared with other experimental data to check the model predictions. The revealed hierarchy effects

on electronic structure of native bone are discussed in section 5.

2. Theoretical

According to the x-ray scattering and microscopic studies the length (L_x), width (L_y) and thickness (L_z) of the crystallites in bone vary in rather wide limits $13 < L_x < 50$ nm, $7 < L_y < 25$ nm and $1.5 < L_z < 4$ nm [1, 24, 37, 38]. To begin with, we neglect the helical shape of the mineralized plate and describe it as a coplanar assembly of the average-size nanocrystallites as plotted in figure 1, middle panel. The average of the experimental sizes [24] allows us to introduce the mean nanocrystallite in bone as a rectangular block with dimensions $\langle L_x\rangle \times \langle L_y\rangle \times \langle L_z\rangle \approx 20 \times 7.5 \times 3.5$ nm^3 and the thickness of the hydrated layer $\langle d\rangle \approx 2$ nm. Comparing the block with the crystallographic cell of HAP we infer that there are about 500 cells and 4×10^4 atoms per crystallite.

Then, the mineralized plate in bone is described as a 3D superlattice assembled from the equal dielectric nanocrystallites separated by the uniform nanolayers. Using the average sizes $\langle L_j\rangle$ and $\langle d\rangle$ we determine the basic vectors of translation $\mathbf{b}_j = \mathbf{L}_j + d$ of the superlattice as ≈22.0, 9.5 and 5.5 nm, where $\mathbf{L}_j = \langle L_j\rangle\vec{j}$ and $\vec{j}$ is the unit vector in Cartesian coordinates. These vectors are shown in figure 1 (middle panel),

Secondly, the nanoblock is described as an extended crystallographic cell assembled in such a way that their coplanar assembly would form the perfect-crystal in case the separating layers disappear. This means that the electronic structure of the 3D superlattice will approach to the band structure of perfect HAP when $\langle d\rangle \to 0$. Thirdly, the cyclic border conditions are applied to describe both the crystallite and their coplanar assembly. These assumptions allow us to reveal regularities in the electronic structure of the mineralized plates and to link it with the band structure of the perfect crystal.

In general case the 3DSL model encounters difficulties because of essential disordering in atomic structure of nanoblocks and nanolayers. To overcome the difficulties, the 'black-boxes' concept [39] is applied and the suggested model is reformulated in terms of the 3D superlattice of 'black nanoboxes in muddy waters'. In its framework we step over the uncertainty in atomic positions by using integral electro-optical characteristics of the nanocrystallites and nanolayers. This enables us to inspect changes in electronic structure associated with transition from the single-crystal to the coplanar assembly.

The dispersion $E(k)$ of electronic states of the 'black-boxes'-assembly as a function of $\langle d\rangle$ and $\langle L\rangle$ obeys the equation [39]

$$e^{2ikb_j} - 2\,\mathrm{Re}\left(\frac{1}{T(E;\,\langle d\rangle,\,\langle L\rangle_j)}\right)e^{2ikb_j} + 1 = 0. \qquad (1)$$

It describes the relationship between the electronic structure of a periodic system and the integral electro-optical characteristic (T) of its cell taken separately and assigns the certain energy E to the electron wave number k. In the case under study $T(E;\langle d\rangle,\langle L\rangle)$ is the amplitude of electron transmission through the supercell. In general case the amplitude is determined by interference of the incident electron wave and the scattered ones on atoms belonging to the supercell and depends on the amplitudes T' and T'' of the waves transmitted (forward scattered) through and reflected (back scattered) from the crystallite and the hydrated layer. This approach has been previously used to study the electronic structure of encapsulated molecules [40].

To simplify equation (1), the effects of multiple scattering of electron waves on atoms belonging to both the hydrated layer and the crystallite are neglected. Hence $T \approx T'T''$ and the coefficient in the second term on the left side of equation (1) is

$$\mathrm{Re}\left(\frac{1}{T}\right)_j = \left|\frac{1}{T'_j(\kappa)T''(\kappa)}\right| \cos(\kappa b_j + \tau_j + \gamma). \qquad (2)$$

$\kappa = \sqrt{E}$, $\tau(\kappa)$ and $\gamma(\kappa)$ are the electron phase shifts in the crystallite and the separating layer respectively.

By combining equations (1) and (2) we can describe the distortion of the band structure in the single crystal at transition to the coplanar assembly of the crystallites. This distortion is accompanied by complicated changes, such as emergence of the minibands [41–43] as well as the interferential changes associated with the additional phase shift γ and the transparency weakening as $|T| < |T'|$. The minibands dispersion is not discussed here. We concentrate on the spectral shift and narrowing of the band in HAP which occur in the coplanar assembly of the separated nanoblocks. For narrow bands these changes are especially apparent.

As the center of the n-band is determined by the condition

$$\kappa R_j + \tau + \gamma = \tfrac{\pi}{2} + \pi n \;(n = 0,\ 1,\ 2,\ \ldots) \qquad (3)$$

we predict the red shift δE_n of the band in the assembly and roughly estimate it as

$$E^{(n)}_{\mathrm{ass}} - E^{\{n\}} \equiv \delta E_{3\mathrm{d}} \approx E_{3\mathrm{d}}\frac{\tilde{d}}{\langle L\rangle}. \qquad (4)$$

$E^{(n)}$ and $E^{(n)}_{\mathrm{ass}}$ are the band energy in the single crystal and the corresponding energy in the assembly, R_j denotes the crystallographic parameters (a, b, c) of HAP, $\tilde{d}$ is the electron-optical length of the separating layer and $\langle L\rangle$ is the average size of the nanocrystallite. According to the 3DSL model, the shift δE_n is originated by the super periodicity of the coplanar assembly and demonstrates linear dependence on both the band energy in the single-crystal and the ratio of the thickness of the spacer layers to the size of the crystallite. The chemical effects are completely ignored to highlight the size dependence of the electronic structure in bone tissue. Within these approximations the red shift δE_n can be attributed to the comprehensive expansion of the assembly as compared with the single crystal. The similar explanation follows from the description of the single nanocrystallite as a quantum dot: the energy of a quantum state decreases with an increase of the

dot radius just as adiabatic expansion leads to a cooling of the electron gas.

The upper and lower bounds of the spectral HAP-to-assembly changes can be found by considering the two limiting cases of empty and opaque separating layers. In the former case, $|T''| = 1$ and $\gamma = -\frac{\kappa d}{N}$ where N is number of elementary cells in the crystallite. Let us evaluate the red shift of the narrow Ca 3d empty band in bone tissue. According to the band structure calculations of HAP [21, 22], the energy $E^{(3d)} \approx 2$ eV above the bottom of the conduction band. Then, using equation 4 and the sizes of the mean nanocrystallite we estimate $\delta E_{3d} \approx 0.4$ eV. In addition to the red shift, the narrowing of the band in the assembly is also expected. In the later limiting case the transparency of the separating layer and the phase shift γ come to zero, hence, no shift appears and the band approaches the quasidiscrete level.

The 3DSL model predicts the size-dependent spectral changes in electronic structure of mineralized phase relative to the band structure of HAP. The size distribution of the crystallites and their mean size are age-related functions and are controlled by higher-lying hierarchical levels. Thus, one can speak about the hierarchy-induced size-dependent effects in electronic structure of bone.

3. Experimental

To visualize the hierarchy-induced effects the high resolution x-ray absorption measurements of native bone are performed. Powdered and sliced bone samples were used as objects. They were derived from cortical middle third of the femur, tibia and humerus from three white mongrel male rats weighing 180–220 g. Cortex has been thoroughly cleaned of soft tissue, washed in saline, dried with blotting paper, and then either sliced into thin plates 15×10 mm^2 in size or ground to fine powder with particles of size ~1 mkm.

The NEXAFS studies on the powder samples were carried out using monochromatic synchrotron radiation at the D1011 beamline at the MAX II electron storage ring (the MAX IV laboratory, Lund University, Sweden) [44]. The samples for absorption measurements were prepared *ex situ* in air by rubbing powders into the scratched surface of copper plates 5×5 mm^2 in size. The substrate surfaces were cleaned mechanically and by sonication in ethanol. All measurements of absorption spectra were performed under ultrahigh vacuum conditions with a residual gas pressure in the experimental chamber ~10^{-9} mbar. The samples were placed at the angle of ~45° with respect to the incident beam of the monochromatic radiation and the size of the focal spot on the sample was around 1×1 mm^2. The NEXAFS spectra at the Ca 2p, P 2p and O 1s thresholds of the bone samples were measured by recording the total electron yield (TEY) as a function of incident photon energy. It is well known that the electron yield near the x-ray absorption edge is proportional to the absorption cross section [45, 46]. The TEY spectra were acquired by measuring the drain current from the sample and characterized by probing depths of >10 nm. All the x-ray absorption spectra were recorded with a photon-energy resolution of 50 meV for the P 2p edge (photon energy $h\nu \sim 140$ eV), 100 meV for the Ca 2p edge ($h\nu \sim 350$ eV) and 200 meV for the O 1s edge ($h\nu \sim 535$ eV). The spectra were normalized to the incident photon flux, which was monitored by recording the TEY from a clean gold mesh mounted in the beamline (in front of the sample). The photon energy $h\nu$ over the range of the O1s, Ca 2p and P 2p absorption spectra was calibrated against the first narrow peak in the F 1s and Ti $2p_{3/2}$ absorption spectra of solid K_2TiF_6 (F 1s → t_{2g}, 683.9 eV and Ti $2p_{3/2}$ → t_{2g}, 459.0 eV [47]) as well as in the C 1s absorption spectrum of solid C_{60} (C 1s → LUMO, 284.5 eV [48]), respectively.

The NEXAFS measurements of sliced samples were carried out at the Polarimeter station at UE56/2 PGM beamline at the BESSY II synchrotron light source at the Helmholtz-Zentrum Berlin using s-polarized synchrotron radiation [49, 50]. The spectra were collected by monitoring the TEY from the samples in a current mode. The samples were placed at an angle of ~45° with respect to the incident beam of the monochromatic radiation. GaAsP diodes were used as x-ray detectors with a Keithley 617 electrometer as a current meter. The efficiency of the detector was taken into account. The absolute energy calibration was carried out by measuring the energies of the reference N_2 lines as well as of the absorption edges for iron filter in the first and higher orders of diffraction. The attained energy resolution was better than $E/\Delta E = 3000$ with the accuracy of the energy scale of about 10 meV.

No sample charging or decomposition effects due to the intense beam of soft x rays were detected for powder and sliced samples during the measurements. The spectra were recorded several times from different points of the sample and their absorption structures have usually shown a good reproducibility.

4. NEXAFS analysis

4.1. Ca 2p edge

Figure 2 (left panel) presents the measured Ca 2p NEXAFS spectra of the powder and sliced native bone in curves 1 and 2, respectively. For comparison, the digitalized Ca 2p NEXAFS spectrum of HAP measured in [31] is also plotted in the figure (curve 3). Both their close similarity and distinct changes are clearly visible. The similarity is determined by the intense lines A and B and low intense peaks a_1, a_2 and b that dominate in the NEXAFS spectra. These resonance features can be attributed to the multiplet splitting of the Ca^{2+} $2p^53d^1$ electron configuration in the weak crystal field examined previously in [51]. At the same time, the red shift ≈1 eV of the features relative to those in HAP determines the distinct deviation of Ca $2p_{1/2,3/2}$ → 3d transition energies in bone and HAP. Taking into account that the Ca 2p hole relaxation in bone and HAP is nearly the same we infer that the density of Ca^{2+} 3d states in bone is also shifted downward relative to the 3d-subband in HAP. In addition to the red shift

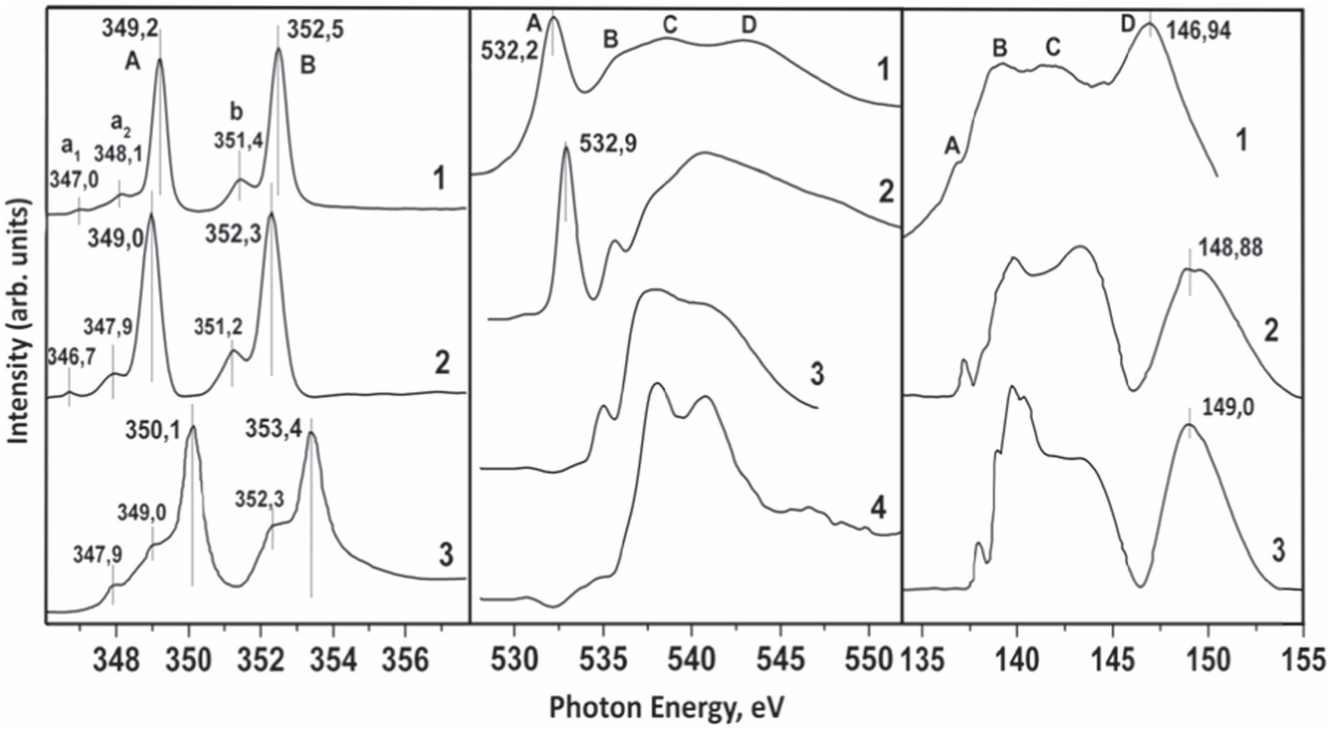

Figure 2. Left panel: Ca 2p NEXAFS of powder (1) and sliced (2) native bone, and HAP (3) [31]. Central panel: O 1s NEXAFS of native bone powder (1), (2)–(4) refer to dried bone [31], liquid water [52] and HAP [31]. Right panel: P 2p NEXAFS of native bone powder (1), and heated (400 °C) bone (2) and HAP (3) [31]. In each panel the NEXAFS spectra are normalized to integral intensity for better comparison.

the 3d-states distribution is narrower in bone. Our line shape analysis of curves 1 and 3 in the left panel gives the full-width-at-half-maximum (FWHM) of the lines A and B equal respectively to 0.48 and 0.56 eV in native bone and to 0.60 and 1.19 eV in HAP. Thus, the experimental data analysis supports the predicted band distortion in HAP at transition to the mineralized bone and allows us to link it with super periodic organization of the latter.

Such a strong shift ≈1 eV detected for the Ca $2p_{1/2,3/2} \rightarrow 3d$ transition energies in native bone relative to HAP is rather a surprise. To verify it the spectral positions of the lines A and B in native bone (curves 1 and 2 in the left panel) have been compared with the transition energies in HAP averaged over the several experimental measurements [31–34]. The averaged shift $\langle \delta E_{3d} \rangle \approx 0.6$ eV agrees reasonably with our model expectation.

4.2. O 1s edge

Figure 2 (central panel) presents the measured O 1s NEXAFS of the native bone powder (curve 1). This spectrum is compared with the O 1s NEXAFS spectra of dried (in a jet of compressed air) bones (curve 2) and HAP (curve 4) measured by Rajendran *et al* [31] and liquid water (curve 3) obtained by Cappa *et al* [52]. Substantial changes in the x-ray absorption spectra are clearly visible.

The intense and rather narrow line *A* at 532.2 eV and the complex broad band *B–C–D* starting from 535 eV and extending up to 550 eV dominate in the O 1s NEXAFS in native bone. Examining the low energy line *A* we see that it is resident in the O 1s absorption of native and dried bones, but strongly suppressed in bone heated up to 400 °C and does not exist in HAP (curve 4) [31]. The O 1s NEXAFS of heated bones demonstrates close resemblance with HAP (curve 4) and $CaCO_3$ and $Ca_3(PO_4)_2$ [31, 53]. As bone heating above 200 °C leads to the removal of the intercrystallite water [19, 20] the line *A* could be attributed to oxygen absorption in the hydrated layer. This conclusion is supported by the IR spectroscopic studies (see e.g. [54, 55]). Those studies evidence that bone heating suppresses the broad band centered at 3400 cm^{-1} tightly related with O–H vibrations. But the lowest absorption line in the O 1s absorption spectrum of liquid water (curve 3) emerges only at 535 eV [52]. Therefore the line *A* cannot be directly assigned with x-ray transitions in the intercrystallite water.

To understand the origin of the line *A* we firstly take into account the fundamental ion–water interactions [56, 57]. In this case the line *A* can be assigned with the O 1s absorption in the hydroxyde anion OH^- in aqua solutions [58–60]. Upon addition of KOH or NaOH to water, new spectral features emerge respectively at 532.5 eV [60] or 532.8 eV [59]. Cappa *et al* [60] have assigned the low-energy feature with the O 1s-to-valence transition in the $OH^-(H_2O)_m$ anion. The resonant Auger spectroscopic studies [59] have confirmed this assignment. According to the computations [60] the OH^- ion exists with a predominately 'hyper-coordinated' solvation shell. This spectral change results primarily from direct electronic perturbation of the unoccupied molecular orbitals of surrounding water molecules. The line A could be also assigned with O 1s absorption in $Ca^{2+}(H_2O)_n$. Since the electronic structures of the $Mg^{2+}(H_2O)_n$ and $Ca^{2+}(H_2O)_n$

clusters are very similar one may assume the resonance behavior at 532 eV in $Ca^{2+}(H_2O)_n$. This behavior could be induced either by the superlattice effect on H_2O in the hydrated layer or by the water adsorption on the crystallites.

Secondly, the line *A* can be associated with O 1s absorption in the collagen molecules. The experimental and theoretical investigations [61–65] show that the O 1s $\rightarrow \pi^*$ transitions in carboxyl group (O–C==O), carbonyls H_2CO and $(CH_3)_2CO$ are located in the vicinity 530.8–532.3 eV. In the third, the line *A* is contributed by the O 1s $\rightarrow \pi^*$ transitions in the $[PO_4]^{2-}$ or $[PO_4]^{-}$ clusters with the unsaturated P–O bond [53].

Thus, the intense resonance at 532.2 eV (central panel, curve 1) has a complicated origin. It can be attributed to x-ray absorption in aqua solution and adsorbed water inside the hydrated layer and in the collagen. Having clarified its origin we will get the key to understand the fundamental interactions between the water in the hydrated nanolayers and collagen in bone tissue.

As for the broad band *B–C–D* in curve 1, it is evidently determined by the O 1s transitions in $[PO_4]^{3-}$ located in the crystallites and the hydrated layers. As a consequence of the composite origin of the main resonance features in the O 1s NEXAFS their HAP-to-bone spectral changes are not discussed.

4.3. P 2p edge

The right panel in figure 2 presents the measured P 2p NEXAFS spectrum of the native bone powder (curve 1). Its comparison with the P 2p NEXAFS of heated bones up to 400 °C (curve 2) and HAP (curve 3) obtained in [31] demonstrates their close resemblance though the resonance features *A–D* are less pronounced in the spectrum of native bone.

The P 2p NEXAFS is determined by the series of transitions from the deep P $2p_{1/2,3/2}$ levels to the pre-edge a_1(P3s), t_2(P3p) and the quasibound e^*(Pεd) and $t_2{}^*$(Pεd) molecular-like states spatially localized within the tetrahedron cage $[PO_4]^{3-}$ [66, 68]. Their close similarity with the Si 2p NEXAFS of the isoelectronic and isostructural SiF_4 molecule and $[SiO_4]^{2-}$ molecular-like group [68, 69] can be mentioned. The P $2p^{-1}{}_{3/2,1/2}$ e^* and $t_2{}^*$ states located above the edge are usually attributed to the shape resonances (see, e.g. [67]).

The P 2p NEXAFS of native and heated bone and HAP [31, 53] provides an additional sensitive probe of the hierarchy induced changes in electronic structure of bone tissue. First of all, the comparison of the P 2p NEXAFS makes evident the HAP-to-bone red shifts. Considering the low energy band *A* in curve 2 and 3 we see that the P $2p_{3/2} \rightarrow a_1$(P3s) transitions energy 138.04 eV in HAP decreases to 137.15 eV in heated bone. The observed large HAP-to-bone red shift $\delta E_{P3s} \approx 0.9$ eV confirms its relation with the effect of super periodicity on the band structure of HAP. This assignment is also supported by the recent investigation [67], where it is shown that, in contrast to the shape resonances, the pre-edge states in molecular solids and crystals containing chemical stable molecular-like groups demonstrate minor sensitivity to the surroundings of the core-excited atom. Regrettably our measurements of native bone (curve 1) do not allow resolving the band *A*.

The red shift of the high energy line *D* assigned with the P 2p $\rightarrow t_2{}^*$(Pεd) shape resonance is clearly visible. Comparing curves 1 and 3 we observe the HAP-to-bone red shift $\delta E_{P\varepsilon d} \approx 3.06$ eV. The transition energy 149.0 eV (curve 3) in HAP varies up to 146.94 eV (curve 1) in native bone. Considering the P 2p NEXAFS in different $[PO_4]^{3-}$-containing compounds [66] one may see that the resonance energies vary much weaker. The significant shift $\delta E_{P\varepsilon d}$ can be explained by using equation (4) and taking into account that the P εd-states of HAP are located much higher than Ca^{2+} 3d states relative to the bottom of the conductive band. Since the P 2p-hole relaxation is nearly the same in bone and HAP, the density of the P 3s and continuous εd-states demonstrate similar red shift relative to those in HAP. The FWHM of the line *D* is not discussed because the P 2p $\rightarrow t_2{}^*$(Pεd) transition is triply degenerated and its changes can be motivated by both the decrease in transparency of the supercell and its splitting due to the point group symmetry reduction.

5. Discussion and conclusion

The theoretical and experimental investigations have shown that in bone tissue there exists a close relationship between its hierarchical organization and local electronic structure of its mineralized phase. To reveal the hierarchy induced changes in electronic structure, the 3DSL model is introduced. The mineralized bone is described as a superlattice composed from uniformly sized nanocrystallites. $20 \times 7.5 \times 3.5$ nm^3 of HAP separated one from another by the hydrated layer with 2nm thickness. Having considered the interplay of short-, long- and super-range order parameters we have predicted the specific changes in electronic structure of the mineralized phase compared with the single-crystal HAP. It is shown that the HAP-to-bone red shift is a product of the band energy in HAP and the ratio of the thickness of the separated layer to the crystallite size. In the framework of the model the electronic structure of the mineralized phase is approaching to the band structure of the single-crystal HAP when the ratio comes to nil. Further development of the 3SDL model is evidently required. In the first turn we suppose to take into account imperfect atomic structure of the crystallites and helical shape of their assemblies. The recent calculations [70] have demonstrated the effect of crystallites orientation on Ca 1s NEXAFS in bone.

There exists a dependence of the crystallite size on the development of tissue structures (see, e.g. [71]). According to the 3DSL model, the size-dependent ratio $\tilde{d}/\langle L \rangle$ is the important tool for functionalizing the electronic structure of the mineralized bone. For example, the average size of nanocrystallites in young postnatal bovine bone $9 \times 6 \times 2$ nm^3 is much smaller than that in mature bone measured by the same method [71]. It is also known that brittle bones of mature animals or animals with osteoporosis contain relatively large and uniformly sized nanocrystallites, while young bone comprises small crystallites [72]. By equation (2) the

HAP-to-bone red shift is hence predicted to be much larger for young bone than for mature bone and can be attributed to the hierarchy-induced size-dependent effect on the ground material.

To visualize the predicted hierarchy-induced changes in electronic structure we have measured spectral distributions of oscillator strength for x-ray transitions near the Ca and P 2p and O 1s edges in native bone and revealed the HAP-to-bone spectral deviations. Their analysis has shown that the Ca and P 2p NEXAFS spectra of native bone and HAP demonstrate close similarity in the number and relative intensity of the resonance features and their distinct spectral shifts. Whereas the O 1s NEXAFS spectra of native bone and HAP differ substantially.

The HAP-to-bone changes in the Ca and P 2p NEXAFS develop themselves as the shifts of the Ca^{2+} $2p^53d^1$, P $2p^{-1}a_1$(P3s) and P $2p^{-1}t_2^*$(Pεd) excitations as well as the narrowing of the white lines *A* and B that refer to the Ca $2p_{1/2,3/2} \rightarrow 3d$ transitions. The red shifts δE_{Ca3d}, δE_{P3s} and $\delta E_{P\varepsilon d} \approx 0.6$ eV, 0.85 eV and 3.06 eV describe the influence of the super periodicity on the band structure of HAP and are assigned with the hierarchy-induced effect on the ground level in bone tissue.

The HAP-to-bone changes in the O 1s NEXAFS have demonstrated its more complicated behavior conditioned mainly by the effect of the intercrystallite water. We have attributed the lowest O 1s-to-valence excitation at 532.2 eV in native bone to the O 1s transitions in (i) hydroxide $OH^-(H_2O)_m$ anions and $Ca^{2+}(H_2O)_n$ cations in the hydrated nanolayers, (ii) the carboxyl groups in the collagen and (iii) $[PO_4]^{m-}$ anions with unsaturated P–O bonds ($m = 1$ and 2), but surprisingly not to HAP or liquid water. As for the broad band *B–D* in the O 1s NEXAFS spectrum of native bone it is assigned with superposition of electronic transitions in $[PO_4]^{3-}$ and water. Further investigations of spectral distribution of oscillator strength for O 1s transitions in native bone as well as in molecular-like fragments, such as $OH^-(H_2O)_m$, $Ca^{2+}(H_2O)_n$, carboxyl, $[PO_4]^{2-}$, $[PO_4]^-$, are needed for deeper understanding the hierarchy-induced effects on the intercrystallite water.

Finally we note that the 3DSL model gives us a key for understanding relationships between hierarchical organization of bone tissue and the local electronic structure of the mineralized phase and spectral distribution of oscillator strength for core-to-valence transitions in it. In addition to the difference in the elemental composition of HAP and bioapatite, the size distribution of the nanocrystallites in mineralized bone influences its electronic structure and opens a way to functionalize its chemical and physical properties. Fine tuning of ion exchange processes in bone is impossible without further theoretical and experimental investigations of the hierarchy-induced changes in electronic structure. We also note that x-ray absorption spectroscopy (including various differential methods) provides a sensitive probe of local electronic structure and hierarchical organization of bone.

Acknowledgments

The authors acknowledge the RFBR grant 15-02-06369 and St. Petersburg State University grant 11.38.261.2014.

References

[1] Weiner S and Wagner H D 1998 *Annu. Rev. Mater. Sci.* **28** 271–98
[2] Currey J 2001 *Nature* **414** 699
[3] Buehler M 2007 *Nanotechnology* **18** 295102
[4] Avrunin A S, Tikhilov R M, Abolin A B and Shcherback I G 2005 *Morfologiia* **2** 78–82 (in Russian)
[5] Avrunin A S, Tihilov R M, Shubniakov I I, Parshin L A, Melnikov B E and Pliev D G 2010 *Morfologiia* **6** 69–75 (in Russian)
[6] Fratzl P and Weinkamer R 2007 *Prog. Mat. Sci.* **52** 1263–334
[7] Neuman W F and Neuman M W 1958 *The Chemical Dynamics of Bone Mineral* (Chicago: University of Chicago Press)
[8] Hancox M N 1972 *Biology of Bone* (Cambridge: Cambridge University Press)
[9] Currey J 1984 *The Mechanical Adaptation of Bones* (Princeton, NJ: Princeton University Press)
[10] Bertazzo S and Bertran C A 2006 *Key Eng. Mater.* **309–311** 3–6
[11] Gautieri A, Vicentini S, Redaelli A and Buehler M 2011 *Nano Lett.* **11** 757–66
[12] Dorozhkin S V 2015 *J. Funct. Biomater.* **6** 708–832
[13] Reiche I, Lebon M, Chadefaux C, Muller K, Anne-Solenn H, Gensch M and Schade U 2010 *Anal. Bioanal. Chem.* **397** 2491–9
[14] Chadefaux C, Vignaud C, Chalmin E, Robles-Camacho J, Arroyo-Cabrales J, Johnson E and Reiche I 2009 *Am. Miner.* **94** 27–33
[15] Knothe Tate M L 2007 Engineering of functional skeletal tissues *Topics in Bone Biology* vol 3 (London: Springer) pp 141–60
[16] Currey J D 1964 *Biorheologi* **2** 1–10
[17] Zhilkin B A, Denisov-Nikolski Y I and Doktorov A A 2003 *Usp. Sovremennoy Biologii* **123** 590–8 (in Russian)
[18] Avrunin A S, Tihilov R M, Parshin L K and Shubniakov I I 2008 *Traumatologiya Ortopediya Rossii* **2** 77–83 (in Russian)
[19] Wopenka B and Pasteris J D 2005 A mineralogical perspective on the apatite in bone *Mater. Sci. Eng.* C **25** 131–43
[20] Yoder C H, Pasteris J D, Worcester K N and Schermerhorn D V 2012 *Calcif. Tissue Int.* **90** 60–7
[21] Rulis P, Ouyang L and Ching W Y 2004 *Phys. Rev.* B **70** 155104
[22] Matsunaga K and Kuwabara A 2007 *Phys. Rev.* B **75** 014102
[23] Denisov-Nikolski Y I, Mironov S P and Omeljanenko N P 2005 *Actual Problems of Theoretical and Clinical Osteoartrology* (Moscow: Novosti)
[24] Avrunin A S, Denisov-NIkolsky Y I, Doktorov A A, Krivosenko Y S, Samoilenko D O, Pavlychev A A and Shubniakov I I 2015 *Traumatologiya Ortopediya Rossii* **3** 37–50 (in Russian)
[25] Legros R, Balmain N and Bonel G 1987 *Calcif. Tissue Int.* **41** 137–44
[26] Bertazzo S, Bertran C A and Camilli J A 2006 *Key Eng. Mater.* **309–311** 11–4
[27] Frank-Kamenetskaya O, Koltsov A, Kuzmina M, Zorina M and Poritskaya L 2011 *J. Mol. Struct.* **992** 9–18
[28] Penel G, Leroy G, Rey C and Bres E 1998 *Calcif. Tissue Int.* **63** 475–81
[29] Stöhr J 1992 *NEXAFS Spectroscopy* (Berlin: Springer)

[30] Koningsberger D C, Prins R, Bianconi A and Durham P J 1988 *X-Ray Absorption: Principles, Applications, Techniques of EXAFS, SEXAFS, and XANES* (New York: Wiley)

[31] Rajendran J, Gialanella S and Aswath P B 2013 *Sci. Eng.* C **33** 3968–79

[32] Naftel S J, Sham T K, Yiu Y M and Yates B W 2001 *J. Synchrotron Radiat.* **8** 255–7

[33] Cosmidis J, Benzerara K, Nassif N, Tyliszczak T and Bourdelle F 2015 *Acta Biomater.* **12** 260–9

[34] Eiden-Assmann S and Wiertanhaus M 2000 In-Situ XANES Spectroscopy at the Ca K edge of calcium phosphate compounds (http://hera.physik.uni-konstanz.de/oldmaret/publications/publ/2000_Eiden_In-Situ%20XANES%20Spectroscopy.pdf)

[35] Eisa M H, Shen H, Mi Y, Ibrahim K and Khalid M H 2011 *J. Sci. Tech.* **12** 109–17

[36] Wang C, Eisa M H, Jin W, Shen H, Mi Y, Gao J, Zhou Y, Yao H and Zhao Y 2008 *Nucl. Instrum. Methods Phys. Res.* B **266** 1619–22

[37] Wilson E E, Awonusi A, Morris M D, Kohn D H, Tecklenburg M M J and Beck L W 2005 *J. Bone Miner. Res.* **20** 625–34

[38] Danilchenko S N 2007 *Visnik SumDU (Proceedings of SumDU)* vol 2 (*Seriya Fizika, matematika, mekhanika (Series of Physics, Mathematics, Mechanics)*) pp 33–59

[39] Heine V 1970 *Solid State Phys.: Adv. Res. Appl.* **24** 1–36

[40] Brykalova X O, Rostov D A, Krivosenko Y S and Pavlychev A A 2014 *J. Electron Spectrosc. Relat. Phenom.* **196** 71–4

[41] Keldysh L V 1962 *Sov. Phys-Solid State* **4** 1658–61

[42] Capasso F, Mohammed K and Cho A Y 1986 *IEEE J. Quantum Electron.* **QE-22** 1853–69

[43] Lazarenkova O L and Balandin A A 2001 *J. Appl. Phys.* **89** 5509–15

[44] Nyholm R, Svensson S, Nordgren J and Flodström A 1986 *Nucl. Instrum. Methods Phys. Res.* A **246** 267–71

[45] Lukirskii A P and Brytov I A 1964 *Sov. Phys-Solid State* **6** 43–53

[46] Gudat W and Kunz C 1972 *Phys. Rev. Lett.* **29** 169–72

[47] Vinogradov A S, Fedoseenko S I, Krasnikov S A, Preobrajenski A B, Sivkov V N, Vyalikh D V, Molodtsov S L, Adamchuk V K, Laubschat C and Kaindl G 2005 *Phys. Rev.* B **71** 045124

[48] Brühwiler P A, Maxwell A J, Nilsson A, Whetten R L and Mårtensson N 1992 *Chem. Phys. Lett.* **193** 311–6

[49] Schaefers F *et al* 1997 *App. Opt.* **38** 4074–88

[50] Gaupp A, Schaefers F, MacDonald M, Uschakow S, Salashchenko N N and Gaykovich P P 2013 *J. Phys.: Conf. Ser.* **425** 122013–6

[51] de Groot F M F, Fuggle J C, Thole B T and Sawatsky G A 1990 *Phys. Rev.* B **41** 928–37

[52] Cappa C D, Smith J D, Wilson K R and Saykally R J 2008 *J. Phys. Condens. Matter* **20** 205105

[53] Yang S, Wang D, Liang G, Yiu Y M, Wang J, Sun X and Sham T K 2012 *Energy Environ. Sci.* **5** 7007–16

[54] Rajendran J 2011 XANES and FTIR study of dried and calcined bones *Master Thesis* The University of Texas at Arlington

[55] Mkukuma L D, Skakle J M S, Gibson I R, Imrie C T, Aspden R M and Hukins D W L 2004 *Calcif. Tissue Int.* **75** 321–8

[56] Headrick J M, Diken E G, Walters R S, Hammer N I, Christie R A, Cui J, Mishakin E M, Duncan M A, Johnson M A and Jordan K D 2005 *Science* **308** 1765–9

[57] Robertson W H, Diken E G, Price E A, Shin J W and Johnson M A 2003 *Science* **299** 1367–72

[58] Megyes T, Bálint S, Grósz T, Radnai T, Bakó I and Sipos P 2008 *J. Chem. Phys.* **128** 044501

[59] Aziz E F, Ottosson N, Faubel M, Hertel I V and Winter B 2008 *Nature* **455** 89–91

[60] Cappa C D, Smith J D, Messer B M, Cohen R C and Saykally R J 2006 *J. Phys. Chem.* B **110** 5301–9

[61] Nuevo M, Milam S N, Sanford S A, De Gregorio B T, Cody G D and Kilcoyne A L D 2011 *J. Adv. Space Res.* **48** 1126–35

[62] Gordon M L, Cooper G, Morin C, Araki T, Turci C C, Kaznatcheev K and Hitchcock A P 2003 *J. Phys. Chem.* A **107** 6144–59

[63] Remmers G, Domke M, Puschmann A, Mandel T, Xue C, Kaindl G, Hudson E and Shirley D A 1992 *Phys. Rev.* A **46** 3935–44

[64] Triguero L, Pettersson L G and Agren H 1998 *Phys. Rev.* B **58** 8097–110

[65] Hitchcock A P and Brion C E 1980 *J. Electron Spectrosc. Relat. Phenom.* **19** 231–50

[66] Yin Z, Kasrai M, Banckroft G M, Tan K H and Feng X 1995 *Phys. Rev.* B **51** 742–50

[67] Flesch R, Serdaroglu E, Brykalova X O, Kan E I, Klushina E S, Krivosenko Y S, Pavlychev A A and Rühl E 2013 *J. Chem. Phys.* **138** 144302

[68] Pavlychev A A, Vinogradov A S, Zimkina T M, Onopko D E and Titov S A 1982 *Opt. Spectrosc.* **52** 506–9

[69] Miron C, Guillemam R, Leclercq N, Morin P and Simon M 1998 *J. Electron Spectrosc. Relat. Phenom.* **93** 95–103

[70] Hesse B *et al* 2016 *Anal. Chem.* **88** 3826–35

[71] Tong W, Glimcher M J, Katz J L, Kuhn L and Eppell S J 2003 *Calcif. Tissue Int.* **72** 592–8

[72] Taylor A J, Rendina E, Smith B J and Zhou D H 2013 *Chem. Phys. Lett.* **588** 124–30